Simultaneous near-field and far-field imaging of the 11.9-nm Ni-like Sn soft-x-ray laser

F. Staub,* M. Braud, and J. E. Balmer
Institute of Applied Physics, Sidlerstrasse 5, 3012 Bern, Switzerland

J. Nilsen and S. Bajt
Lawrence Livermore National Laboratory, Livermore, California 94551, USA
(Received 30 March 2004; published 28 July 2004)

We report on two-dimensional near-field imaging experiments of the 11.9-nm Sn x-ray laser that were performed with a set of Mo/Y multilayer mirrors having reflectivities of up to ~45% at normal and at 45° incidence. Second-moment analysis of the x-ray laser emission was used to determine values of the x-ray beam propagation factor M^2 for a range of irradiation parameters. The results reveal a reduction of M^2 with increasing prepulse amplitude. The spatial size of the output is a factor of ~2 smaller than previously measured for the 14.7-nm Pd x-ray laser, while the distance of the x-ray emission with respect to the target surface remains roughly the same.

DOI: 10.1103/PhysRevA.70.013813 PACS number(s): 42.55.Vc, 42.60.Jf

I. INTRODUCTION

Since the first demonstration of substantial x-ray laser gain in neonlike selenium [1], the electron-collisional excitation scheme has proven to be the most successful method on the route towards high output power and saturated gain. Saturated operation of soft-x-ray lasers is important because it assures the maximum stimulated-emission power extraction from a given volume of excited plasma. Clear evidence of saturation has been reported in the last few years by a number of authors for the $4d \rightarrow 4p$, $J=0-1$ transition in nickel-like elements at wavelengths between 14.7 and 7.3 nm [2–4]. The efficiency with which saturation is achieved in the Ni-like lasers has recently been improved by exploiting the prepulse and multiple-pulse techniques [5–7] and, on the other hand, by reducing the pump pulse duration to the picosecond range, combined with travelling-wave irradiation [8–10]. Reports on the properties of these lasers have included measurements of the output energy, pulse duration, near- and far-field intensity distributions, and divergence [11]. The recent development of Mo/Y multilayer x-ray mirrors [12] has opened up a wavelength range from 7 to 12 nm for soft-x-ray imaging experiments not accessible so far. The Mo/Y mirrors allow one to investigate the near-field intensity distributions as well as to perform other imaging experiments of x-ray lasers—and other x-ray sources—below the wavelength of the Si absorption edge around 12.5 nm. Although, in principle, mirrors could be built for the 11–12 nm range using Mo/Be multilayers [13], such mirrors are rarely used because of the toxicity of Be.

In previous experiments, we have demonstrated saturated gain on the $4d \rightarrow 4p$, $J=0-1$ transition in Ni-like Pd, Ag, and Sn at 14.7, 13.9, and 11.9 nm, respectively, with a pump irradiation scheme utilizing a 0.5% prepulse that irradiated flat slab targets 5–6 ns before the main pulse. Both the prepulse and the main pulse had a duration of 100 ps. The output energy of the x-ray laser at saturation was measured to be 5 μJ per beam [14].

In this work we report on a series of simultaneous near-field and far-field imaging experiments for the Sn 11.9-nm x-ray laser using four different prepulse schemes: a 0.5% prepulse at −6 ns, a 2.8% prepulse at −2 ns, an 8% prepulse at −1 ns, and a 16% prepulse at −0.8 ns, with respect to the main pulse at 0 ns. The delay settings chosen correspond to the maxima of the x-ray laser intensity for the specific prepulse amplitudes.

II. EXPERIMENTAL SETUP

The experiments were performed using the 1054-nm Nd:glass laser system at the Institute for Applied Physics of the University of Berne. The laser, having a final amplifier of 90-mm diameter, is capable of delivering up to 40 J at a pulse duration of 100 ps full width at half maximum. The output beam is focused to give a line focus of 2.5-cm length and approximately 100-μm width using a combination of a 500-mm focal length aplanatic doublet and a −1700-mm focal length cylindrical lens. Targets were 25-mm-wide slabs having a diamond-machined surface finish. The ASE x-radiation is emitted from either end of the target along the line focus.

In a first series of experiments, the near-field and far-field intensity distributions were recorded simultaneously using the diagnostics setup shown in Fig. 1(a). It consists of a concave, multilayer, normal-incidence Mo/Y x-ray mirror that images the output aperture at one end of the Sn 11.9-nm laser onto the P43 phosphor/charge coupled device (CCD) camera recording system via a flat normal-incidence Mo/Y mirror. The mirrors are made of up to 60 alternating layer pairs of Mo and Y yielding reflectivities in excess of 40%. The layers have a period of 6.15 nm for normal incidence and 8.97 nm for the 45° mirror, respectively. A detailed description of the multilayers can be found in Ref. [12]. The concave mirror has a radius of curvature of 24 cm and is positioned such as to image the output plane of the Sn

*Electronic address: felix.staub@iap.unibe.ch

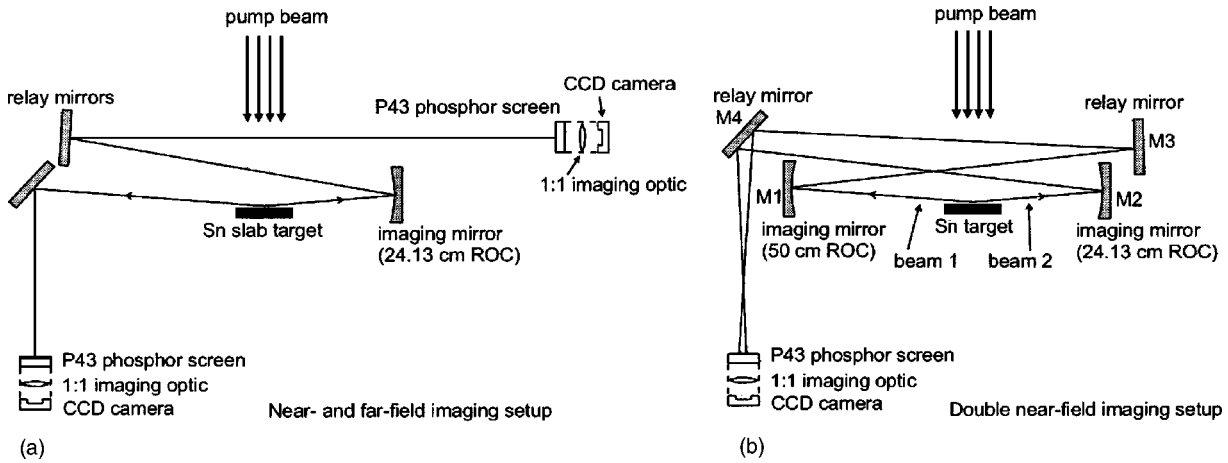

FIG. 1. (a) Experimental setup for near- and far-field imaging. The pump beam irradiates a 2.5-cm-long flat Sn target. The output aperture of the 11.9-nm nickel-like tin laser is imaged onto the P43 phosphor/CCD camera detection system with a magnification of 12. The beam propagating to the left is used for the far-field diagnostics. (b) Experimental setup for double-near-field imaging. The pump beam irradiates a 2.5-cm-long flat Sn target. The output apertures of the 11.9-nm nickel-like tin laser are imaged onto the P43 phosphor/CCD camera detection system with a magnification of 10 and 17, respectively.

laser onto the phosphor screen with a magnification of 12. The overall spatial resolution of this diagnostics was measured to be ~ 2.5 μm at the output plane of the Sn laser, limited by the phosphor and the CCD imaging optics. This value is consistent with the smallest structures that can be resolved in the near-field images. The targets had a 25-μm-diam steel wire placed 145 μm in front of the target surface at this end of the target which served as an absolute spatial fiducial in the measurements. The laser emission from the other end of the target was used to record the far-field intensity distribution at a distance of 2.05 m from the target via a 45° angle-of-incidence Mo/Y turning mirror. The recording system was a similar P43 phosphor/CCD camera combination. The spatial resolution in this case was given by the 23-μm-square pixel size of the CCD camera. In both cases, the P43 phosphors were coated with ~ 120 nm of zirconium to discriminate against background radiation.

The diagnostics setup used for the double-near-field experiments is shown in Fig. 1(b). It consists of two concave, multilayer, normal-incidence Mo/Y x-ray mirrors that image the output apertures at both ends of the Sn 11.9-nm laser onto the P43 phosphor/CCD camera recording system via a flat normal-incidence and a 45° angle-of-incidence Mo/Y mirror. The concave mirrors have radii of curvature of 50 and 24 cm, respectively, and are positioned such as to image the output planes of the Sn laser onto the phosphor screen with a magnification of 10 and 17, respectively. The targets had 25-μm-diam steel wires placed 100 μm in front of the target surface at both ends as absolute spatial fiducials in the measurements.

III. EXPERIMENTAL RESULTS

A. Simultaneous near-field and far-field images

Figure 2 shows typical images of the Sn $J=0-1$ laser emission at 11.9 nm at the output aperture of the target (left) and the simultaneously recorded corresponding far field (right) at a drive irradiance of 10 TW/cm^2 for different prepulse configurations. The plasma blow-off direction is the horizontal axis in the left figure with zero corresponding to the original target surface. The shadow of the fiducial wire is indicated by two lines at the right of the emission zone. The small-scale structures observed in the near-field images are most likely caused by inhomogeneities in the density profile and/or by the different gain lengths experienced by the individual rays. The far-field images show modulations parallel to the target surface, visualized by the contour lines. The origin of these modulations is not clear to date, but may be attributed to coherent rays, spatially overlapping in the gain region, but diverging by $10-20$ μrad, forming an interference pattern in the far-field. The pattern was reproducible for most of the shots for unchanged prepulse conditions, with the strongest modulations observed with the 0.5% prepulse. With increasing prepulse amplitude the modulations of the far-field show a tendency to get weaker and more irregular. The angular frequency and the modulation depth are considerably lower as compared to the interference fringes observed in the far-field beam patterns of Refs. [15,16].

A series of measurements was performed for prepulse amplitudes of 0.5%, 2.8%, 8%, and 16%. We performed a second-moment analysis of the images, in order to obtain the near-field radii Δx and Δy perpendicular and parallel to the target surface, respectively, as well as the divergence semiangles $\Delta\theta_x$ and $\Delta\theta_y$ of the far-field. The nth moments of a beam for the x and θ_x coordinates are defined as follows [17]:

$$\langle x^n\rangle = \frac{\iint x^n I_S(x,y)dxdy}{\iint I_S(x,y)dxdy}, \quad \langle \theta_x^n\rangle = \frac{\iint \theta_x^n I_a(\theta_x,\theta_y)d\theta_x d\theta_y}{\iint I_a(\theta_x,\theta_y)d\theta_x d\theta_y},$$

where $I_S(x,y)$ and $I_a(\theta_x,\theta_y)$ are the near-field and the far-field intensity distributions, respectively. The beam radii and divergence semiangles are then given by

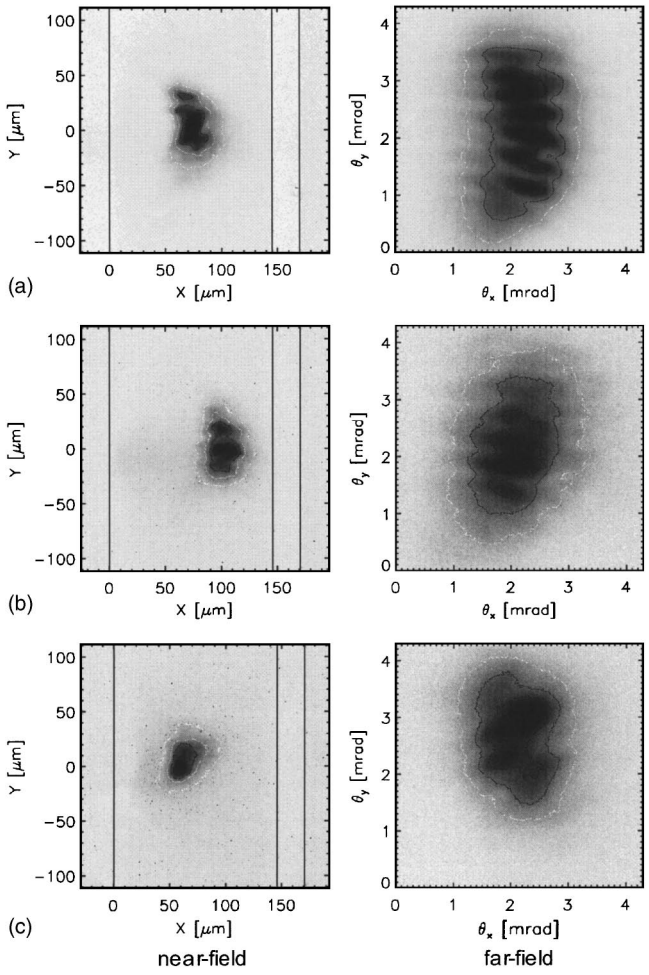

FIG. 2. Near-field images of the 11.9-nm Sn laser emission (left) and simultaneously recorded far fields with a 0.5% prepulse and a 6-ns delay (a), 2.8% prepulse and 2-ns delay (b), and 16% prepulse and 0.8-ns delay (c). The plasma blow-off direction is the horizontal axis. The line at $x=0$ in the left figures corresponds to the original target surface. The shadow of the fiducial wire is indicated by two lines at the right of the emission. The images are overlaid with linearly scaled contour plots.

$$\Delta x = 2\sqrt{\langle x^2\rangle - \langle x^1\rangle^2}, \quad \Delta\theta_x = 2\sqrt{\langle \theta_x^2\rangle - \langle \theta_x^1\rangle^2}.$$

The calculation for the y and θ_y coordinates is analogous.

With the aid of the fiducial wire, the position of the emitting zone was measured. Figure 3 shows a plot of the distance of the emission zone from the original target surface as a function of the prepulse amplitude, together with the results of the Ni-like Pd x-ray laser presented in Ref. [18]. As can be seen, the curve shows a flat maximum at ~ 100 μm from the target for a prepulse amplitude in the range of 3%. For weak prepulses the peak intensity of the Pd laser emission occurs ~ 10 μm closer to the target surface than for Sn.

Figure 4 shows a plot of the geometrical mean radius $(\Delta x \Delta y)^{1/2}$ of the emission zone as a function of the prepulse amplitude. The emission zone for the Pd laser is seen to be a factor of $\sim 1.5-2$ larger than for Sn. The size of the Sn emission decreases linearly from 29×38 μm^2 to 24×26 μm^2 with increasing prepulse amplitude, whereas the

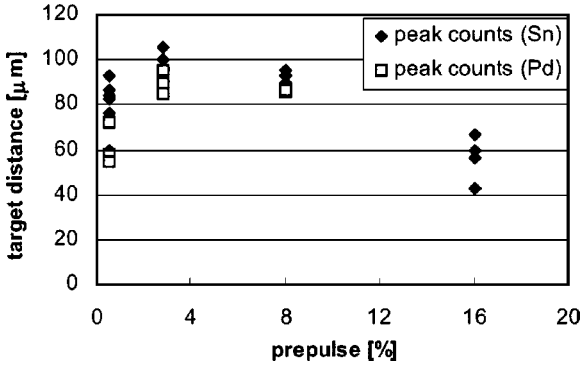

FIG. 3. Distance of the 11.9-nm Sn x-ray laser emission zone from the target as a function of the prepulse amplitude. Results for the 14.7-nm Pd x-ray laser from Ref. [18] are included for comparison.

size of the Pd emission shows a rather nonlinear behavior. Stepping from the 0.5% to the 2.8% prepulse, the size of the Pd laser emission decreases more significantly than for Sn.

The decrease of the mean emission size is mainly due to a decrease of the extent in y direction (parallel to the target surface), which reduces the ellipticity $\Delta y/\Delta x$ of the near field from 1.3 for the 0.5% prepulse to 1.2 for the 16% prepulse. This behavior can also be seen in the left column of Fig. 2. The decrease of Δy with increasing prepulse amplitude may be explained by the short prepulse delay of only 0.8 ns for the 16% prepulse, leaving the plasma less time to expand perpendicularly to the main plasma blow-off direction as compared to the delay of 6 ns for the 0.5% prepulse.

In Fig. 5 the geometrical mean of the divergence semiangle is plotted as a function of prepulse amplitude. The semiangles perpendicular and parallel to the target surface are 1.4×1.8 mrad^2 for the 0.5% prepulse, decreasing to 1.1×1.5 mrad^2 for the 16% prepulse. Compared to Sn, the divergence of the Pd laser is about 1.8 times the value for the 0.5% prepulse given earlier, converging to nearly identical values for the strongest prepulse. As already noticed for the near-field beam radius, in contrast to the Sn laser, the divergence angle of the Pd-laser emission shows a significant decrease stepping from 0.5% to 2.8% prepulse amplitude (Fig. 5), which is mainly caused by the decrease in y direction.

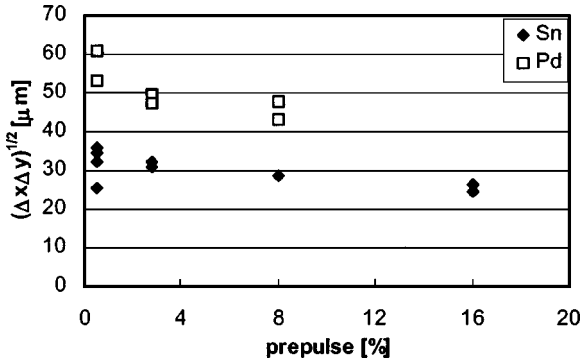

FIG. 4. Mean radius of the near-field intensity distribution based on second moment analysis as a function of the prepulse amplitude. Results for the Pd x-ray laser are included for comparison.

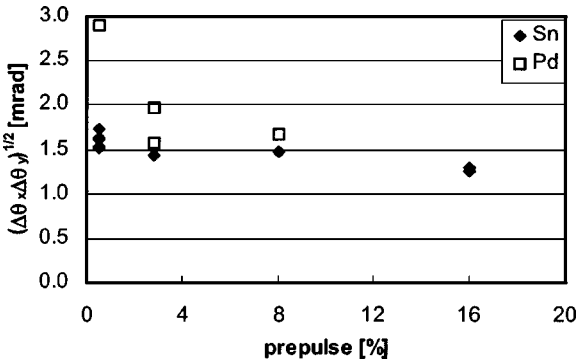

FIG. 5. Mean divergence semiangle obtained from the far-field intensity distributions based on second moment analysis as a function of prepulse amplitude. Results for the Pd x-ray laser are included for comparison.

Assuming the x-ray laser emission characteristics to be similar at both ends of the target, the second-moment analysis of the intensity distributions was used to determine the x-ray laser beam propagation factors, M_x^2 and M_y^2 (Fig. 6), in the directions perpendicular and parallel to the target surface, respectively, for the four prepulse configurations investigated. The beam propagation factors are given by [17]:

$$M_x^2 \equiv \frac{\pi \Delta x \Delta \theta_x}{\lambda}, \quad M_y^2 \equiv \frac{\pi \Delta y \Delta \theta_y}{\lambda}, \quad M^4 \equiv M_x^2 M_y^2,$$

where λ is the laser wavelength.

The values of M^2 are in the range of 10 in the x direction and around 20 in the y direction. For both axes the M^2 shows a slight decrease with increasing prepulse amplitude, although the data are widely spread, especially in the y direction. The ratio M_y^2/M_x^2 decreases from 1.9 for a 0.5% prepulse to 1.6 for 16% prepulse, in coincidence with the observation that the emission region gets more compact and circular with increasing prepulse (cf. Fig. 2). The results of the 8% prepulse are somewhat unique, as they show an above-average ratio M_y^2/M_x^2 with large extents parallel, but small dimensions perpendicular to the target surface. However, in the product $M^4 = M_x^2 M_y^2$ shown in Fig. 7, this irregularity is balanced. Moreover, in Fig. 6 the complete set of data analyzed is plotted, while in Figs. 4, 5, and 7 the results

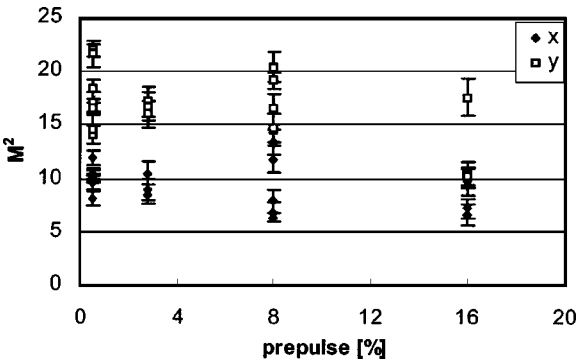

FIG. 6. Beam propagation factors M_x^2 (diamonds) and M_y^2 (open squares) as a function of prepulse amplitude.

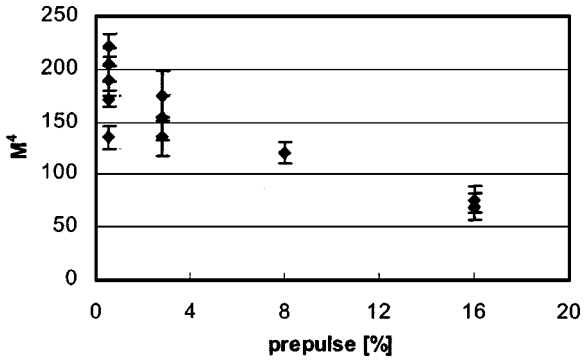

FIG. 7. Sn x-ray laser beam propagation factor $M^4 = M_x^2 M_y^2$ as a function of prepulse amplitude.

are restricted to the most intense shots of each prepulse scheme for the sake of clarity. The value of M^4 is a measure of the maximum number of modes in the lasing region. It decreases from $M^4 \approx 200$ for the weakest prepulse down to $M^4 \approx 70$ for the strongest prepulse. From Figs. 4 and 5 it can be seen that the decrease of M^4 is due to a reduction in both the size of the emitting zone and the divergence of the laser beam. This is consistent with the findings of Ref. [18] for the 14.7 nm Pd x-ray laser.

Figure 8 shows the time integrated laser intensity. The data are obtained from integrating over the far-field beam area and averaging over the shots of identical prepulse amplitudes. The intensity drops significantly for prepulses stronger than 0.5%, in contrast to the Pd x-ray laser, where the intensity is nearly constant for all prepulse configurations used [18]. This could be attributed to the higher electron temperature needed to generate the Ni-like Sn plasma as compared to the lower-Z Ni-like Pd plasma. As the experiments were performed with identical sets of parameters of the pump laser for both elements, the electron temperature would drop more easily below the required level of ionization for Sn than for Pd on changing irradiation parameters.

B. Double near-field measurements

In order to verify that the laser emission characteristics are similar on both ends of the target, the near fields at both ends were recorded simultaneously [setup in Fig. 1(b)]. The

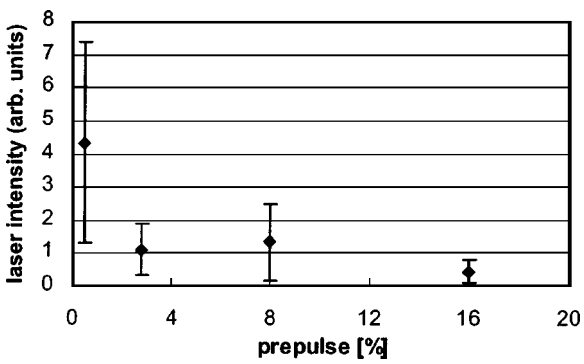

FIG. 8. Sn x-ray laser intensity as a function of prepulse amplitude.

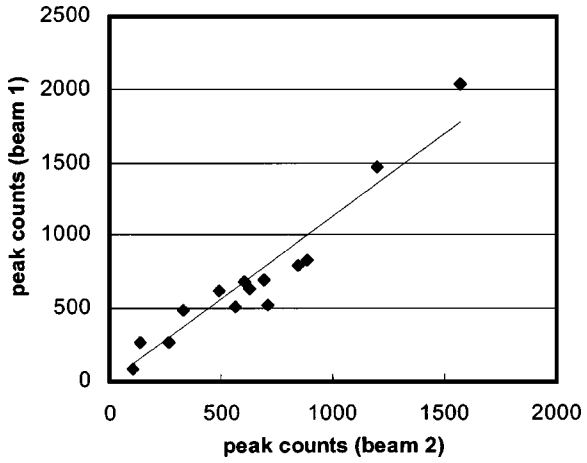

FIG. 9. Peak laser intensities of the two emitting apertures. The linear regression yields a slope of 1.12 and a correlation coefficient of 0.96. The prepulse was fixed at 0.5%, preceding the main pulse by 6 ns.

prepulse was fixed at 0.5%, preceding the main pulse by 6 ns. We found that for most of the shots both near fields are similar in size and orientation while a few rather asymmetric images exhibit more differing intensity distributions.

The data of the double-near-field images were investigated and compared in terms of intensity, spatial extent, and shape. Figure 9 shows the correlation of the peak intensities of the two near fields. The values are corrected for the loss caused by the additional reflection of beam 1 at M3 [see Fig. 1(b)] and the different magnification of the two imaging paths. The linear regression yields a slope of 1.12 and a correlation coefficient of $R=0.96$. The slope is very close to unity, especially in view of the uncertainty of the reflectivity of the additional mirror M3 in beam 1. A reflectivity of 42% was taken from data given in Ref. [12]. The intensity of beam 1 is found to vary by 32% (standard deviation) with respect to beam 2 for the same shot, while the intensities of different shots may vary up to a factor of ~ 10. The residual fluctuations of the intensities of both emitting apertures may be explained by small variations of the intensity distribution of the pump laser along the line focus and irregularities of the target surface.

While the intensities of both emission zones are very well correlated, the fluctuations of the spatial extents of the two emitting apertures with respect to each other are of the same order as the shot-to-shot fluctuations of one single emission zone. Figure 10 shows two pairs of simultaneously recorded near-field images. The images correspond to beam 2 (left column) and beam 1 (right column), respectively [see Fig. 1(b)]. The image pair in Fig. 10(a) shows intensity distributions of rather similar shape and extent on both ends of the target. However, for some shots we observed larger differences in the two emissions [Fig. 10(b)].

On average, beam 1 was found to be emitted ~ 10 μm closer to the target surface than beam 2. This effect might be due to an intensity gradient of the prepulse along the line focus, causing the plasma to expand faster at one end of the target than on the other side. However, the absolute position of the emission has no influence on the moments and does

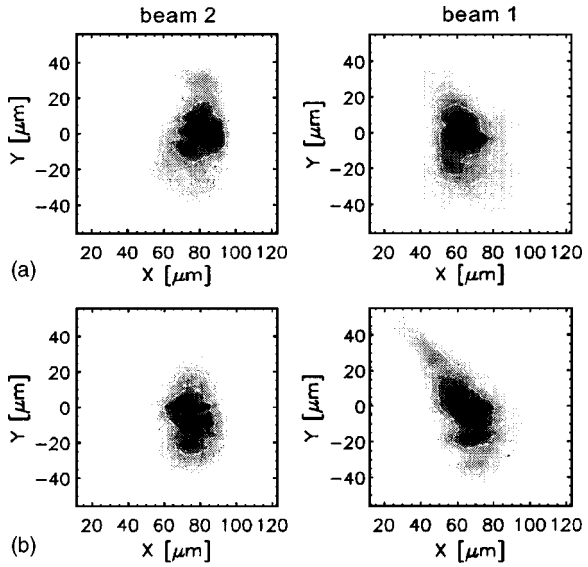

FIG. 10. Simultaneously recorded near-field image pairs using the setup in Fig. 1(b). The images correspond to beam 2 (left column) and beam 1 (right column). The intensity distributions are rather similar in shape and size at both ends of the target (a). In the left image, the fiducial wire cutting off the emission at ~ 100 μm can also be observed. For some shots we observed larger differences in the two emissions (b).

not change the values of the beam propagation factor M^2. Therefore, we may conclude that we introduce no systematical errors using simultaneous near-field and far-field imaging for M^2 determination.

IV. CONCLUSIONS

We have reported a series of simultaneous near-field and far-field imaging experiments for the Ni-like 11.9-nm Sn x-ray laser using Mo/Y multilayer mirrors. The measurements were conducted with the aim to characterize the two-dimensional source intensity distribution and its position relative to the target surface. The images were analyzed in terms of the beam propagation factor, M^2, yielding values in the order of 10–20, and the effect of different prepulse amplitudes was investigated. The distance of the emission zone from the target was found to be of order 60–100 μm, with the largest values obtained for a few-percent prepulse amplitude. Simultaneous imaging of the two emitting apertures allowed us to determine a value of M^2 for every single shot.

ACKNOWLEDGMENTS

The authors would like to thank H. P. Weber for fruitful discussions, B. Locher for expert technical assistance, and W. Lüscher for target preparation. This work was supported in part by the Swiss National Science Foundation. The work of the LLNL authors was performed under the auspices of the U.S. Department of Energy by the University of California Lawrence Livermore National Laboratory under Contract No. W-7405-Eng-48.

[1] D. L. Matthews *et al.*, Phys. Rev. Lett. **54**, 110 (1985).
[2] J. Zhang *et al.*, Phys. Rev. Lett. **78**, 3856 (1997).
[3] J. Zhang *et al.*, Science **276**, 1097 (1997).
[4] R. Tommasini, F. Loewenthal, and J. E. Balmer, Phys. Rev. A **59**, 1577 (1999).
[5] J. Nilsen, B. J. MacGowan, L. B. Da Silva, and J. C. Moreno, Phys. Rev. A **48**, 4682 (1993).
[6] H. Daido *et al.*, Phys. Rev. Lett. **75**, 1074 (1995).
[7] J. E. Balmer, R. Tommasini, and F. Loewenthal, IEEE J. Quantum Electron. **5**, 1435 (1999).
[8] J. Dunn *et al.*, Phys. Rev. Lett. **84**, 4834 (2000).
[9] R. E. King *et al.*, Phys. Rev. A **64**, 053810 (2001).
[10] A. Klisnick *et al.*, Phys. Rev. A **65**, 033810 (2002).
[11] J. Nilsen, J. Zhang, and A. G. MacPhee, Phys. Rev. A **56**, 3161 (1997).
[12] J. Nilsen, S. Bajt, H. N. Chapman, F. Staub, and J. E. Balmer, Opt. Lett. **28**, 2249 (2003).
[13] J. F. Seely, C. Montcalm, S. Baker, and S. Bajt, Appl. Opt. **40**, 5565 (2001).
[14] J. E. Balmer, M. Braud, and C. Siegel, Proc. SPIE **4505**, 93 (2001).
[15] J. Dunn *et al.*, Proc. SPIE **4505**, 62 (2001).
[16] A. Klisnick *et al.*, Proc. SPIE **4505**, 75 (2001).
[17] A. E. Siegman, Proc. SPIE **1224**, 1 (1990).
[18] Ch. Siegel, M. Braud, and J. E. Balmer, Opt. Commun. **210**, 305 (2002).